Optics Letters

Coherence lattices in surface plasmon polariton fields

Yahong Chen,[1,2,*] Andreas Norrman,[3] Sergey A. Ponomarenko,[4] and Ari T. Friberg[1]

[1]Institute of Photonics, University of Eastern Finland, P.O. Box 111, FI-80101 Joensuu, Finland
[2]Center of Light Manipulations and Applications, School of Physics and Electronics, Shandong Normal University, Jinan 250014, China
[3]Max Planck Institute for the Science of Light, Staudtstraße 2, D-91058 Erlangen, Germany
[4]Department of Electrical and Computer Engineering, Dalhousie University, Halifax, Nova Scotia B3 J 2X4, Canada
*Corresponding author: hon2019@163.com

Received 7 May 2018; revised 15 June 2018; accepted 15 June 2018; posted 18 June 2018 (Doc. ID 331122); published 13 July 2018

We explore electromagnetic coherence lattices in planar polychromatic surface plasmon polariton (SPP) fields. When the SPP constituents are uncorrelated—and thus do not interfere—coherence lattices arise from statistical similarity of the random SPP electromagnetic field. As the SPP correlations become stronger, the coherence lattices fade away, but the lattice structure reemerges in the spectral density of the field. The polarization states of the structured SPP lattice fields are also investigated. Controllable plasmonic coherence and spectral density lattices can find applications in nanophotonics, such as nanoparticle manipulation.

OCIS codes: (030.1640) Coherence; (240.6680) Surface plasmons; (260.2110) Electromagnetic optics.

https://doi.org/10.1364/OL.43.003429

Optical lattices, constituting periodic variations in the intensity, polarization state, or phase distribution of optical fields [1–4], have been widely studied and advanced in various application areas, such as laser cooling and trapping of neutral atoms [5], lattice light-sheet microscopy [6,7], sorting microscopic particles [8], and photonic crystal engineering [9]. More recently, altogether different types of optical lattices, viz., optical coherence lattices, which refer to optical fields having periodic coherence structures, have been introduced theoretically [10] and realized experimentally [11]. Propagation of optical coherence lattice fields demonstrates that they may lead to promising applications in image transfer and robust free-space optical communications [12,13]. Also, electromagnetic coherence lattices with totally unpolarized three-dimensional polarization states were found in purely evanescent near fields [14].

Surface plasmon polaritons (SPPs) [15] are central to nanophotonics [16] and modern plasmonics [17], spawning a broad range of interdisciplinary science and engineering [18]. To date, plasmonics has mainly involved fully coherent fields, although SPPs are also created by partially coherent light [19]. However, there is now an increasing recognition that partial coherence, as a novel degree of freedom, has a decisive role in controlling the spatial, temporal, and polarization properties of the SPP fields themselves [20–22]. Therefore, tailoring the coherence features of SPPs is of fundamental importance. A crucial step in this direction was taken recently by advancing a framework to customize the electromagnetic coherence of polychromatic SPPs in the Kretschmann geometry [23], and a robust protocol to determine SPP coherence from the scattered far-field spectrum was proposed [24]. Moreover, a coherent-mode decomposition of generic partially coherent SPPs was advanced [25], and planar axicon-like SPP fields of varying states of coherence were analyzed [26]. Such plasmon coherence engineering is expected to be instrumental for creating SPP fields with the desired statistical properties. In this connection, generating SPP coherence lattices presents both fundamental interest and is important with a view on a range of optical arrangements.

In this Letter, we consider the synthesis of electromagnetic coherence lattices in planar, polychromatic surface optical fields composed of partially correlated SPPs in the Kretschmann setup. We call these novel, structured SPP fields of controlled coherence SPP lattice (SPPL) fields. We show that despite lack of interference, uncorrelated SPPs lead to coherence lattices of varying forms through statistical similarity. The electromagnetic coherence lattices embedded in the SPPL field then gradually vanish as the SPP correlations become stronger, only for the lattices to reemerge in the spectral density and the polarization state of the field. The subwavelength periodicity of SPPLs is attractive for many applications, ranging from highly controlled excitation of random molecule or quantum-dot sets (coherence lattices) to nanoparticle trapping (spectral density or polarization lattices). In particular, partially coherent SPPLs can be employed to engineer controllable multiparticle nanoantenna array configurations, which are stable to surface defects and environment fluctuations.

The system at hand, analogous to Kretschmann's setup [15], involves a homogeneous, isotropic, and nonmagnetic metal film deposited on a glass prism in the xy plane (see Fig. 1). The SPPL field at the metal–air interface is composed of $N \geq 2$ SPP modes with the excitation positions distributed uniformly on a circle of radius a and centered at the origin O. We let $\mathbf{r}_{0n} = -a\hat{\mathbf{e}}_n$ be the excitation point of the nth

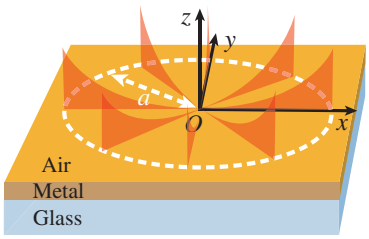

Fig. 1. Schematic illustration of the synthesis of a partially coherent SPPL field. All SPP modes with their excitation points located uniformly on a circle of radius a at the metal–air interface (xy plane) propagate toward the coordinate origin O.

SPP mode that propagates in the direction $\hat{\mathbf{e}}_n = \cos\theta_n\hat{\mathbf{e}}_x + \sin\theta_n\hat{\mathbf{e}}_y$ toward the center O, where $\theta_n = 2\pi(n-1)/N$ is the azimuthal angle with respect to the x axis, and $\hat{\mathbf{e}}_x$ and $\hat{\mathbf{e}}_y$ are the Cartesian x and y unit vectors. The spatial electric part of the SPPL field in air, at point $\mathbf{r}$ and (angular) frequency ω for $(x^2+y^2)^{1/2} \le a$, is then given by

$$\mathbf{E}(\mathbf{r},\omega) = \sum_{n=1}^{N} E_n(\omega)\hat{\mathbf{p}}_n(\omega)e^{i\mathbf{k}_n(\omega)\cdot(\mathbf{r}-\mathbf{r}_{0n})}, \tag{1}$$

where $E_n(\omega)$ is the complex-valued electric-field amplitude of the nth SPP mode at the excitation point. Moreover,

$$\mathbf{k}_n(\omega) = k_t(\omega)\hat{\mathbf{e}}_n + k_z(\omega)\hat{\mathbf{e}}_z, \tag{2}$$

$$\hat{\mathbf{p}}_n(\omega) = \hat{\mathbf{k}}_n(\omega)\times(\hat{\mathbf{e}}_z\times\hat{\mathbf{e}}_n), \tag{3}$$

are the SPP wave and normalized polarization vectors, respectively, with $\hat{\mathbf{e}}_z$ being the Cartesian unit vector in the z direction and $\hat{\mathbf{k}}_n(\omega) = \mathbf{k}_n(\omega)/|\mathbf{k}(\omega)|$ [27]. Note that the wave-vector magnitude $|\mathbf{k}(\omega)|$ is independent of θ_n. We further take the film to be thick enough, so that SPP-mode overlap across the metal can be neglected [28,29]. Thus, the tangential and normal wave-vector components in Eq. (2) read [15]

$$k_t(\omega) = \frac{\omega}{c}\left[\frac{\epsilon_r(\omega)}{\epsilon_r(\omega)+1}\right]^{1/2}, \quad k_z(\omega) = \frac{\omega}{c}\left[\frac{1}{\epsilon_r(\omega)+1}\right]^{1/2}, \tag{4}$$

where $\epsilon_r(\omega)$ denotes the complex-valued relative permittivity of the metal and c is the speed of light.

In view of plasmon coherence engineering [23], the spatial and temporal coherence of the SPPL field can be tailored through modulation of the spectral correlations among the individual SPP modes. To this end, we consider $\mathbf{E}(\mathbf{r},\omega)$ in Eq. (1) as a field realization, and the spectral electric coherence matrix, which encompasses all of the second-order statistical properties of a (stationary) electromagnetic field, is obtained via appropriate averaging [30], i.e., $\mathbf{W}(\mathbf{r}_1,\mathbf{r}_2,\omega) = \langle\mathbf{E}^*(\mathbf{r}_1,\omega)\mathbf{E}^{\mathrm{T}}(\mathbf{r}_2,\omega)\rangle$, where the asterisk, superscript T, and angle brackets denote the complex conjugate, matrix transpose, and ensemble average, respectively. It then readily follows from Eqs. (1)–(3) that

$$\mathbf{W}(\mathbf{r}_1,\mathbf{r}_2,\omega) = e^{-2k_t''(\omega)a}\sum_{n=1}^{N}\sum_{m=1}^{N} W_{nm}(\omega)\mathbf{K}_{nm}(\omega) \times e^{i[\mathbf{k}_m(\omega)\cdot\mathbf{r}_2 - \mathbf{k}_n^*(\omega)\cdot\mathbf{r}_1]}, \tag{5}$$

where $W_{nm}(\omega) = \langle E_n^*(\omega)E_m(\omega)\rangle$ and $\mathbf{K}_{nm}(\omega) = \hat{\mathbf{p}}_n^*(\omega)\hat{\mathbf{p}}_m^{\mathrm{T}}(\omega)$ are the spectral correlation function and the 3×3 polarization-state matrix associated with the nth and mth SPP constituents. Further, $k_t''(\omega)$ is the imaginary part of $k_t(\omega)$, determining the SPP propagation length $l_{\mathrm{SPP}}(\omega) = 1/k_t''(\omega)$. We observe that once the metal parameters, radius a, and mode number N are known, all elements apart from $W_{nm}(\omega)$ are specified in Eq. (5). In other words, the spectral correlation function is an additional degree of freedom that can be exploited, through suitable SPP excitation, to control the physical properties of the SPPL field. This is analogous to the case with copropagating SPPs, for which the spectral correlation function has proven a powerful tool to tailor the field's spatiotemporal coherence state [23].

We consider first the extreme case when all the SPP modes are completely uncorrelated and have equal initial (excitation) intensities $|E_n(\omega)|^2 = |E(\omega)|^2 = I_{\mathrm{SPP}}(\omega)$. The SPP correlation function then becomes $W_{nm}(\omega) = I_{\mathrm{SPP}}(\omega)\delta_{nm}$, with δ_{nm} being the Kronecker delta. Under these conditions, the 3×3 spectral electric coherence matrix in Eq. (5) reduces to

$$\mathbf{W}(\mathbf{r}_1,\mathbf{r}_2,\omega) = I_{\mathrm{SPP}}(\omega)e^{-2k_t''(\omega)a}\sum_{n=1}^{N}\mathbf{K}_{nn}(\omega) \times e^{i[\mathbf{k}_n(\omega)\cdot\mathbf{r}_2 - \mathbf{k}_n^*(\omega)\cdot\mathbf{r}_1]}. \tag{6}$$

To assess the partial coherence of the SPPL field, we use the spectral electromagnetic degree of coherence [30],

$$\mu(\mathbf{r}_1,\mathbf{r}_2,\omega) = \frac{\|\mathbf{W}(\mathbf{r}_1,\mathbf{r}_2,\omega)\|_{\mathrm{F}}}{[\mathrm{tr}\boldsymbol{\Phi}(\mathbf{r}_1,\omega)\mathrm{tr}\boldsymbol{\Phi}(\mathbf{r}_2,\omega)]^{1/2}}, \tag{7}$$

where $\|\cdot\|_{\mathrm{F}}$ is the Frobenius norm, tr denotes the matrix trace, and $\boldsymbol{\Phi}(\mathbf{r},\omega) = \mathbf{W}(\mathbf{r},\mathbf{r},\omega)$ is the (spectral) polarization matrix. The quantity in Eq. (7), obeying $0 \le \mu(\mathbf{r}_1,\mathbf{r}_2,\omega) \le 1$, is a measure of the correlations at ω among all electric-field components at the two spatial points. The upper and lower limits correspond to full coherence and complete lack of coherence. It now follows from Eqs. (2), (3), (6), and (7) that the degree of coherence for the "uncorrelated SPPL field" of Eq. (6), at points $\mathbf{r}_1 = 0$ and $\mathbf{r}_2 = \mathbf{r}$, becomes

$$\mu^2(\mathbf{r},\omega) = \frac{1}{N} + \frac{2\sum_{n=1}^{N-1}\sum_{m=n+1}^{N}\xi_{nm}(\mathbf{r},\omega)}{N\sum_{n=1}^{N}\xi_{nn}(\mathbf{r},\omega)}, \tag{8}$$

where the space–frequency dependent function is

$$\xi_{nm}(\mathbf{r},\omega) = \left[\frac{1+\kappa^2(\omega)\cos\Delta\theta_{nm}}{1+\kappa^2(\omega)}\right]^2 e^{-k_t''(\omega)(C_{nm+}x+S_{nm+}y)} \times \cos[k_t'(\omega)(C_{nm-}x + S_{nm-}y)] \tag{9}$$

with $C_{nm\pm} \equiv \cos\theta_n \pm \cos\theta_m$, $S_{nm\pm} \equiv \sin\theta_n \pm \sin\theta_m$, $\Delta\theta_{nm} = 2\pi(n-m)/N$, $\kappa(\omega) = |k_z(\omega)|/|k_t(\omega)|$, and $k_t'(\omega)$ being the real part of $k_t(\omega)$.

Note that $\mu(\mathbf{r},\omega)$ in Eq. (8) is independent not only of the height z but also of the circle radius a, which effectively merely scales the general electric coherence matrix $\mathbf{W}(\mathbf{r}_1,\mathbf{r}_2,\omega)$ in Eq. (5). Hence, the spatial coherence distribution of SPPL fields is stable. For instance, the uncorrelated SPPL field is highly coherent near the center even when the radius a is large and the SPP modes are strongly attenuated. This is evidenced in Fig. 2, illustrating the spatial behavior of $\mu(\mathbf{r},\omega)$ for an uncorrelated SPPL field at an Ag–air interface ($z=0$) at free-space wavelength $\lambda = 632.8$ nm with different numbers of SPP modes. The plots show clearly that the electromagnetic

degree of coherence has a lattice-like, subwavelength structure with periodic rotational symmetry. When the mode number N is very large, the coherence lattice evolves into an axicon-field-like distribution (a Bessel-correlated SPP field [26]). The variation of $\mu(\mathbf{r},\omega)$, which might appear counterintuitive as the SPP modes are uncorrelated and thus do not interfere, is a result of statistical similarity of the field [31,32].

Moreover, we find from Fig. 2 and Eq. (8) that $\mu(0,\omega) < 1$, indicating that the SPPL field at the center is not fully self-coherent [30]. The physics behind this result lies in the polarization state of the uncorrelated SPPL field. It is specified by the 3×3 polarization matrix, obtained from Eq. (6) as

$$\mathbf{\Phi}(\mathbf{r},\omega) = I_{\mathrm{SPP}}(\omega)\mathrm{e}^{-2[k_t''(\omega)a + k_z''(\omega)z]}\sum_{n=1}^{N}\mathbf{K}_{nn}(\omega)\xi_{nn}(\mathbf{r},\omega), \quad \textbf{(10)}$$

where $k_z''(\omega)$ is the imaginary part of $k_z(\omega)$. The ratio of tangential to normal components of $\mathbf{\Phi}(\mathbf{r},\omega)$ reads

$$\frac{\mathbf{\Phi}_{xx}(\mathbf{r},\omega) + \mathbf{\Phi}_{yy}(\mathbf{r},\omega)}{\mathbf{\Phi}_{zz}(\mathbf{r},\omega)} = \kappa^2(\omega), \quad \textbf{(11)}$$

with $\kappa(\omega) = |k_z(\omega)|/|k_t(\omega)|$ as before. For typical plasmonic metals (e.g., Ag and Au), we have $\kappa(\omega) \ll 1$ in the red part of the visible spectrum [33], whereby Eq. (11) implies that the uncorrelated SPPL field is highly polarized in the z direction. Nevertheless, the field will acquire a significant tangential component toward the blue part of the spectrum (although the normal component remains dominant). If one considers only the tangential field, its polarization state can be analyzed in terms of the four Stokes parameters [30] $S_j(\mathbf{r},\omega) = \mathrm{tr}[\mathbf{\Phi}_t(\mathbf{r},\omega)\boldsymbol{\sigma}_j]$ with $j \in (0,\ldots,3)$, where $\mathbf{\Phi}_t(\mathbf{r},\omega)$ is the 2×2 polarization matrix in the transverse plane, $\boldsymbol{\sigma}_0$ is the 2×2 unit matrix, and $\boldsymbol{\sigma}_1$, $\boldsymbol{\sigma}_2, \boldsymbol{\sigma}_3$ are the three Pauli matrices. The degree of polarization $P(\mathbf{r},\omega)$ of the tangential field reads $P^2(\mathbf{r},\omega) = \sum_{j=1}^{3} s_j^2(\mathbf{r},\omega)$ with $s_j(\mathbf{r},\omega) = S_j(\mathbf{r},\omega)/S_0(\mathbf{r},\omega)$ [30].

The top panels in Fig. 3 show the spatial behavior of $P(\mathbf{r},\omega)$ for the tangential component of the uncorrelated SPPL field at an Ag–air interface ($z = 0$) at $\lambda = 632.8$ nm with different N. The distributions indicate that the tangential fields are partially polarized at the circle's edge, with the maxima of $P(\mathbf{r},\omega)$ at the SPP excitation positions, and gradually become unpolarized at the center, i.e., $P(0,\omega) = 0$. Due to this unpolarized contribution the SPPL field is not completely self-coherent [30] and therefore $\mu(0,\omega) < 1$ in Fig. 2. We also observe that $P(\mathbf{r},\omega)$ is notably less than one at the edge when N is large; for the degree of polarization to reach unity, the radius would have to be much larger than the actual SPP propagation length $l_{\mathrm{SPP}}(\omega)$ [26]. The Stokes parameters $S_j(\mathbf{r},\omega)$ with $j \in (1,2,3)$ characterize the fully polarized part of the field. For the tangential component, it is found from Eqs. (9) and (10) and the definition of the Stokes parameters that $S_3(\mathbf{r},\omega) = 0$, implying that the fully polarized part is linearly polarized. The bottom panels in Fig. 3 illustrate the spatial behavior of the azimuth angle $\varphi(\mathbf{r},\omega) = (1/2)\arctan[S_2(\mathbf{r},\omega)/S_1(\mathbf{r},\omega)]$ of the linear polarization for the tangential component of the uncorrelated SPPL field. We observe that the polarized parts at the SPP excitation positions point toward the circle's center, and with the increase in the SPP-mode number N the polarization state of the polarized field contributions gradually becomes indistinguishable from the radially polarized state.

The correlations (and strengths) of the individual SPP modes can be modified by the technique of plasmon coherence engineering [23]. Radially propagating SPPs may also be launched by other means [26]. As the SPP correlations become stronger, the electromagnetic coherence and spectral density structures of the SPPL field naturally change. In the extreme limit of fully correlated SPP modes, the spectral correlation function in Eq. (5) factors as $W_{nm}(\omega) = E_n^*(\omega)E_m(\omega)$ and the coherence lattices disappear due to complete coherence. However, the lattices will remarkably reemerge in the spectral density of the "correlated SPPL field" due to beating among the SPP modes. The spectral density for a correlated SPPL field is obtained from the electric field $\mathbf{E}(\mathbf{r},\omega)$ in Eq. (1) as $S(\mathbf{r},\omega) = |\mathbf{E}(\mathbf{r},\omega)|^2$, and on taking the SPPs to be in phase and of equal initial intensity $I_{\mathrm{SPP}}(\omega)$ we end up with

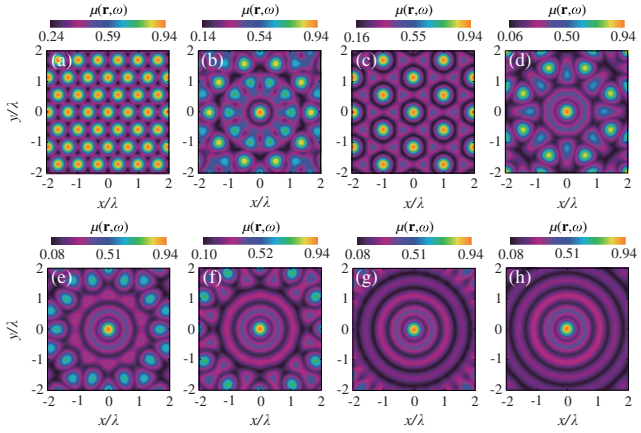

Fig. 2. Spatial behavior of the electromagnetic degree of coherence $\mu(\mathbf{r},\omega)$ for uncorrelated SPPL fields at an Ag–air interface at the free-space wavelength $\lambda = 632.8$ nm with (a) $N = 3$, (b) $N = 5$, (c) $N = 6$, (d) $N = 8$, (e) $N = 10$, (f) $N = 12$, (g) $N = 15$, and (h) $N = 20$ SPP modes. Empirical data are used for Ag [33].

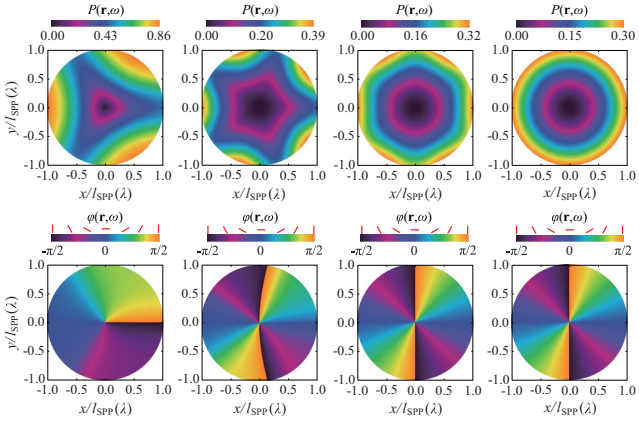

Fig. 3. Spatial behavior of the degree of polarization $P(\mathbf{r},\omega)$ (top panels) and the azimuth angle $\varphi(\mathbf{r},\omega)$ (bottom panels) of the linear polarization state related to the tangential component of the uncorrelated SPPL field at an Ag–air interface at free-space wavelength $\lambda = 632.8$ nm with $N = 3$ (left column), $N = 5$ (second column), $N = 6$ (third column), and $N = 20$ (right column) SPP modes. The red lines above the color bars in the bottom panels show the corresponding polarization orientations, and $l_{\mathrm{SPP}}(\lambda)$ is the SPP propagation length. The relative permittivity of Ag is from empirical data [33].

$$S(\mathbf{r},\omega) = I_{\mathrm{SPP}}(\omega)\mathrm{e}^{-2[k_i''(\omega)a+k_z''(\omega)z]}\left[\sum_{n=1}^{N}\xi_{nn}(\mathbf{r},\omega) + 2\sum_{n=1}^{N-1}\sum_{m=n+1}^{N}\frac{1+\kappa^2(\omega)}{1+\kappa^2(\omega)\cos\Delta\theta_{nm}}\xi_{nm}(\mathbf{r},\omega)\right]. \quad (12)$$

The top panels of Fig. 4 illustrate the spatial behavior of $S(\mathbf{r},\omega)$ at an Ag–air interface ($z = 0$) for $\lambda = 632.8$ nm and $a = I_{\mathrm{SPP}}(\omega)$ of the correlated SPPL field with different N. As expected, the spectral densities show similar subwavelength lattice distributions as the electromagnetic degree of coherence in the uncorrelated SPPL field. Moreover, in the bottom panels of Fig. 4, we show the corresponding ratios $\eta(\mathbf{r},\omega)$ between the normal and tangential contributions to the spectral density, i.e., $\eta(\mathbf{r},\omega) = \Phi_{zz}(\mathbf{r},\omega)/[\Phi_{xx}(\mathbf{r},\omega) + \Phi_{yy}(\mathbf{r},\omega)]$ [cf. Eq. (11)]. The over-exposed areas in the figure stand for $\eta(\mathbf{r},\omega) > 10$; thereby, the fields in these regions are highly polarized in the z direction, whereas the fields are tangentially polarized in the regions with $\eta(\mathbf{r},\omega) \to 0$. We also observe that the polarization state of the correlated SPPL field switches rapidly between the spectral density maxima and minima, where the fields are polarized in the normal and tangential directions, respectively, a clear signature of subwavelength polarimetric structure.

In summary, we have introduced a novel class of statistically stationary, partially coherent, structured SPPL fields that can be established by plasmon coherence engineering through an appropriate superposition of radially propagating SPP modes at a metal–air interface. In particular, electromagnetic coherence lattices with subwavelength structure and partially polarized field states were found in polychromatic SPPL fields composed of uncorrelated SPPs. We also demonstrated that with the increase of the spectral correlations among the SPP modes, the lattice structure transfers from the electromagnetic coherence to the spectral density and the polarization state of the SPPL fields. Such SPPL distributions may find applications in controlled near-field nanoparticle excitation studies.

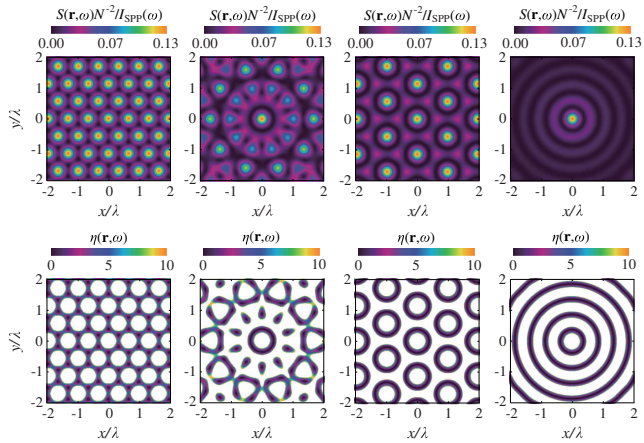

Fig. 4. Spatial behavior of the spectral density $S(\mathbf{r},\omega)$ (top panels) and the ratio $\eta(\mathbf{r},\omega)$ (bottom panels) of the normal and tangential spectral density contributions to the correlated SPPL field at an Ag–air interface at the free-space wavelength $\lambda = 632.8$ nm with $N = 3$ (left column), $N = 5$ (second column), $N = 6$ (third column), and $N = 20$ (right column) SPP modes. The excitation circle radius is equal to the SPP propagation length. Note that $S(\mathbf{r},\omega)$ in the top panels is normalized with respect to the initial SPP intensity $I_{\mathrm{SPP}}(\omega)$ and the mode number N squared. The over-exposed areas in the bottom panels stand for $\eta(\mathbf{r},\omega) > 10$. Empirical data [33] are used for the relative permittivity of Ag.

Funding. Natural Sciences and Engineering Research Council of Canada (NSERC); Academy of Finland (310511); China Scholarship Council (CSC); Swedish Cultural Foundation in Finland; Joensuu University Foundation.

REFERENCES

1. P. Senthilkumaran and R. S. Sirohi, Opt. Commun. **105**, 158 (1994).
2. S. Vyas and P. Senthilkumaran, Appl. Opt. **46**, 2893 (2007).
3. R. W. Schoonover and T. D. Visser, Phys. Rev. A **79**, 043809 (2009).
4. Y. Wang, Y. Xu, X. Feng, P. Zhao, F. Liu, K. Cui, W. Zhang, and Y. Huang, Opt. Lett. **41**, 1478 (2016).
5. I. Bloch, J. Dalibard, and S. Nascimbene, Nat. Phys. **1**, 23 (2005).
6. E. Betzig, Opt. Express **13**, 3021 (2005).
7. B. C. Chen, W. R. Legant, K. Wang, L. Shao, D. E. Milkie, M. W. Davidson, C. Janetopoulos, X. S. Wu, J. A. Hammer III, Z. Liu, B. P. English, Y. Mimori-Kiyosue, D. P. Romero, A. T. Ritter, J. Lippincott-Schwartz, L. Fritz-Laylin, R. D. Mullins, D. M. Mitchell, J. N. Bembenec, A. C. Reymann, R. Böhme, S. W. Grill, J. T. Wang, G. Seydoux, U. S. Tulu, D. P. Kiehart, and E. Betzig, Science **346**, 1257998 (2014).
8. M. P. MacDonald, G. C. Spalding, and K. Dholakia, Nature **426**, 421 (2003).
9. D. N. Christodoulides, F. Lederer, and Y. Silberberg, Nature **424**, 817 (2003).
10. L. Ma and S. A. Ponomarenko, Opt. Lett. **39**, 6656 (2014).
11. Y. Chen, S. A. Ponomarenko, and Y. Cai, Appl. Phys. Lett. **109**, 061107 (2016).
12. L. Ma and S. A. Ponomarenko, Opt. Express **23**, 1848 (2015).
13. X. Liu, J. Yu, Y. Cai, and S. A. Ponomarenko, Opt. Lett. **41**, 4182 (2016).
14. A. Norrman, T. Setälä, and A. T. Friberg, Opt. Lett. **40**, 5216 (2015).
15. S. A. Maier, *Plasmonics: Fundamentals and Applications* (Springer, 2007).
16. L. Novotny and B. Hecht, *Principles of Nano-Optics*, 2nd ed. (Cambridge University, 2012).
17. A. A. Maradudin, J. R. Sambles, and W. L. Barnes, eds., *Modern Plasmonics* (Elsevier, 2014).
18. J. Zhang, L. Zhang, and W. Xu, J. Phys. D **45**, 113001 (2012).
19. D. Morrill, D. Li, and D. Pacifici, Nat. Photonics **10**, 681 (2016).
20. S. Aberra Guebrou, J. Laverdant, C. Symonds, S. Vignoli, and J. Bellessa, Opt. Lett. **37**, 2139 (2012).
21. J. Laverdant, S. Aberra Guebrou, F. Bessueille, C. Symonds, and J. Bellessa, J. Opt. Soc. Am. A **31**, 1067 (2014).
22. A. Norrman, T. Setälä, and A. T. Friberg, Opt. Express **23**, 20696 (2015).
23. A. Norrman, S. A. Ponomarenko, and A. T. Friberg, Europhys. Lett. **116**, 64001 (2016).
24. Y. Chen, A. Norrman, S. A. Ponomarenko, and A. T. Friberg, Opt. Lett. **42**, 3279 (2017).
25. H. Mao, Y. Chen, S. A. Ponomarenko, and A. T. Friberg, Opt. Lett. **43**, 1395 (2018).
26. Y. Chen, A. Norrman, S. A. Ponomarenko, and A. T. Friberg, Phys. Rev. A **97**, 041801 (2018).
27. A. Norrman, T. Setälä, and A. T. Friberg, Opt. Lett. **38**, 1119 (2013).
28. A. Norrman, T. Setälä, and A. T. Friberg, Opt. Express **22**, 4628 (2014).
29. A. Norrman, T. Setälä, and A. T. Friberg, Phys. Rev. A **90**, 053849 (2014).
30. A. T. Friberg and T. Setälä, J. Opt. Soc. Am. A **33**, 2431 (2016).
31. S. A. Ponomarenko, H. Roychowdhury, and E. Wolf, Phys. Lett. A **345**, 10 (2005).
32. T. Voipio, T. Setälä, and A. T. Friberg, J. Opt. Soc. Am. A **32**, 741 (2015).
33. E. D. Palik, ed., *Handbook of Optical Constants of Solids* (Academic, 1998).